Chapter 4

Elastic fields due to surface roughness

4.1 Experimental observation of ex- and intrusions

A single dislocation moving out of a grain at the free surface leaves a surface step. Multiple of these events produce intrusions and extrusions, which continue to grow with continuing load cycles. Basinski and Basinski [5] found that extrusions and intrusions in copper single crystals have the same size and shape, and that the rate of growth decreases after around 10^4 cycles. This decrease in the rate of growth is accompanied by cross slip. Later in the fatigue life, secondary slip is observed. Therefore, many ex- and intrusions develop during fatigue.

It has also been observed by Basinski and Basinski [5] that PSBs develop. Inside a PSB, dislocation motion is strongly localized compared to the matrix surrounding the PSB, which leads to a pronounced roughness at the free surface, commonly referred to as protrusion. This protrusion generally consists of extruded material. If more material is extruded than intruded in a PSB, the volume increases while the density decreases, as confirmed by volume measurements.

The increase in the volume of a PSB can be explained by the production of vacancies inside the persistent slip band (cf. vacancy dipole models in chapter 1) and therefore a swelling of the material. This is generally believed to originate from the formation of dipoles during cyclic deformation. These dipoles may collapse into vacancies/interstitials, if the dipole height is smaller than a critical value. Since the formation energy of vacancies is much lower than that of interstitials more vacancy than interstitial dislocation dipoles collapse. Therefore, more vacancies than interstitials are produced and this leads to swelling of the material.

The difference in the formation energy of vacancies versus interstitials is an effect of the core of the dislocations since the long-range attraction forces for interstitial and vacancy dipoles are identical. Since dislocation dynamics only takes the long-range fields into account, as many vacancy as interstitial dipoles on average will be produced during the simulation. Therefore, no protrusion is formed at the surface in the simulation. However, ex- and intrusions do develop as a consequence of discrete dislocations leaving the grain.

Surface steps cause singular stress concentrations, which according to St. Venant's principle decay over distances on the order of the geometric disturbance. The region influenced by a single surface step is therefore small, i.e. on the order of the Burgers vector of the dislocation producing the surface step. However, as more dislocations leave the crystal the ex- and intrusions may accumulate and therefore the area influenced by the surface roughness increases.

Our model does not take the change in geometry of the material into account since a small strain formulation is used. A finite strain formulation would be needed to capture the evolving surface steps. The basics of the finite strain formulation were developed by Deshpande et al. [49], but the numerics to deal with the continuous change of surface shape are awaiting numerical implementation, e.g. mesh refinement. Therefore, we give an analytical approximation to the elastic fields caused by the surface roughness in this chapter.

4.2 Representative surface step

4.2.1 Introduction

To incorporate the effect of the surface steps, superposition is used for the stress and the displacement fields. Therefore, the interaction of surface steps is neglected in this approach. The total elastic stress is the sum of the stresses as described in chapters 2 or 5 ($\tilde{\boldsymbol{\sigma}} + \hat{\boldsymbol{\sigma}}$) and a contribution $\bar{\boldsymbol{\sigma}}$ due to the surface roughness. The surface roughness itself can be seen as an accumulation of surface steps of different step height, each leading to stress fields $\bar{\boldsymbol{\sigma}}_l$, so that

$$\begin{aligned} \boldsymbol{\sigma} &= \tilde{\boldsymbol{\sigma}} + \hat{\boldsymbol{\sigma}} + \bar{\boldsymbol{\sigma}} \\ &= \tilde{\boldsymbol{\sigma}} + \hat{\boldsymbol{\sigma}} + \sum_l \bar{\boldsymbol{\sigma}}_l \end{aligned} \tag{4.1}$$

Since this is an elastic calculation, the stress fields caused by each step are self similar. If one would increase the geometrical dimensions of the problem, i.e. increase the surface step height, one would proportionally increase the size of the area affected by the surface step. Therefore, it is not necessary to determine the elastic fields for different surface step heights but only to compute the elastic fields for a representative surface step and scale all

lengths by the step height h, as shown in figure 4.1. There, the stress is applied parallel to the free surface, which is divided in an upper and lower terrace.

Moreover, the elastic fields at each point scale linearly with the applied stress; without the applied stress, there is no stress singularity. Hence the field $\boldsymbol{\sigma}_l$ caused by a step of height h_l must be of the form $\boldsymbol{\sigma}_l = \sigma_{\mathrm{app}} \boldsymbol{f}(x_p/h_l)$ with the function $\boldsymbol{f}$ to the determined from elasticity theory.

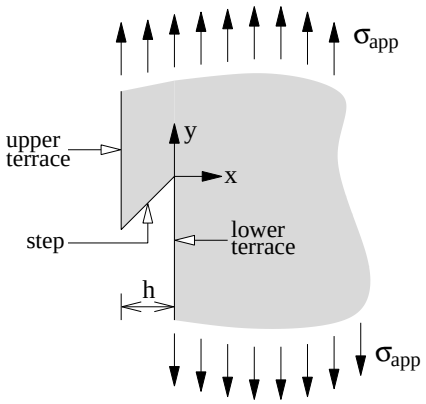

Figure 4.1: Definitions used for the surface step.

To calculate the stress concentration caused by a surface step, three different approaches for a representative surface step are studied in the following subsections and compared to two solutions given in literature. After that, the model which most closely agrees to the numerical solution is studied in more detail.

Since we search for the singular terms of the elastic fields due to the surface step, all stress plots in this chapter show only the singular term $\bar{\sigma}$ of equation (4.1) and call it σ, for simplicity.

4.2.2 Reference calculation with FEM

To compare and validate the solutions of the different approximations, a plane strain finite element calculation of a discrete surface step is executed and the results are verified with mesh refinement for convergence. Figure 4.2 shows for the representative surface step the distribution of the normal stresses in the x- and the y-direction σ_{xx} and σ_{yy}, respectively. This step has a height $h = 1\mu\mathrm{m}$ and an angle of 45° and is embedded in a $200\mu\mathrm{m} \times 200\mu\mathrm{m}$ block. A remote stress $\sigma_{yy} = \sigma_{\mathrm{app}}$ is applied to the block. Due to the different lengths of the upper and lower boundary the applied stresses are different at these sides. However, this difference is small due to the huge difference between the block size and the step height. The applied stress is subtracted from the stress distribution calculated by FEM, and the

resulting stress is the singular term caused by the surface step. The stress distribution for the $6\mu\mathrm{m} \times 6\mu\mathrm{m}$ core of the block is shown in figure 4.2.

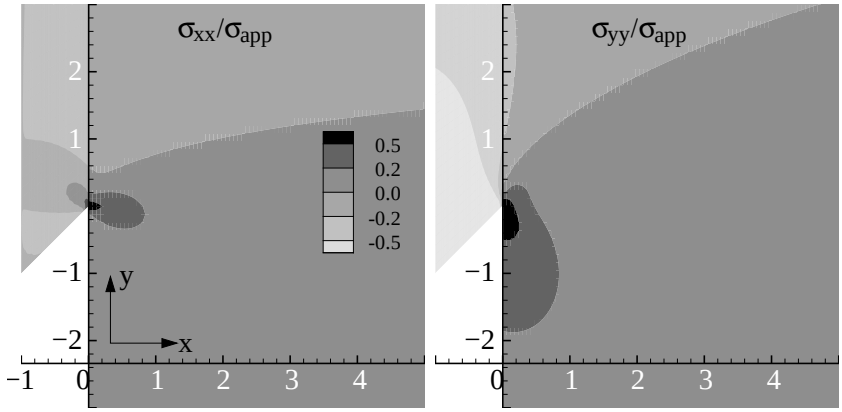

(a) (b)

Figure 4.2: Stress components σ_{xx} (a) and σ_{yy} (b) for a representative surface step in a $200 \times 200\mu\mathrm{m}$ block subjected to a remote stress $\sigma_{yy} = \sigma_{\mathrm{app}}$ calculated by FEM. This step has a height $h = 1\mu\mathrm{m}$ and an angle of $45°$.

4.2.3 Approximation based on the wedge solution with homogeneous boundary conditions

Figure 4.3 illustrates the first approach to solve the elastic problem of a surface step analytically. Here, the stress field caused by the surface step is approximated by the asymptotic field of a wedge in infinite space. The definitions of the local coordinate systems and angles for an infinitely long wedge with an opening angle of $2(\pi - \alpha)$ are shown in figure 4.4.

We try to find the elastic fields of a surface step using the Airy stress function Φ and use the following solution to the governing equation $\Delta^2\Phi = 0$:

$$\Phi = r^{\lambda+1} f(\theta) \tag{4.2}$$

with

$$\begin{aligned} f(\theta) &= c_1 \sin[(\lambda+1)\theta] + c_2 \cos[(\lambda+1)\theta] \\ &+ c_3 \sin[(\lambda-1)\theta] + c_4 \cos[(\lambda-1)\theta]\,. \end{aligned} \tag{4.3}$$

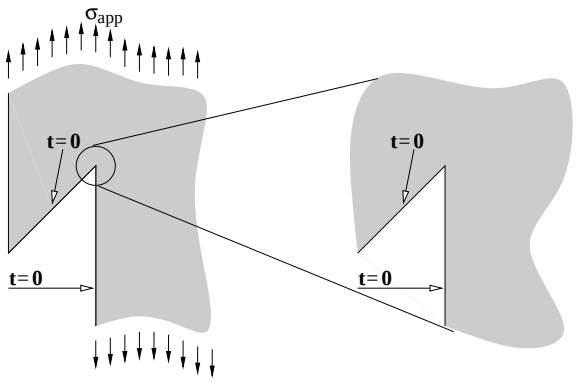

Figure 4.3: First approach to approximate the elastic fields of a surface step.

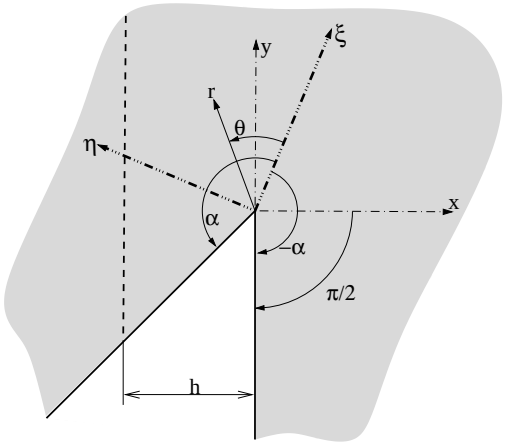

Figure 4.4: Definitions used for the solution of an infinitely long wedge.

Then, the stress components in cylindrical coordinates (figure 4.4) are given by

$$\begin{aligned}\sigma_{\theta\theta} &= \frac{\partial^2\Phi}{\partial r^2} \\ &= r^{\lambda-1}(\lambda+1)\lambda\Big[c_1\sin[(\lambda+1)\theta] + c_2\cos[(\lambda+1)\theta] \\ &\quad + c_3\sin[(\lambda-1)\theta] + c_4\cos[(\lambda-1)\theta]\Big];\end{aligned} \tag{4.4}$$

$$\begin{aligned}\sigma_{rr} &= \frac{1}{r^2}\frac{\partial^2\Phi}{\partial\theta^2}+\frac{1}{r}\frac{\partial\Phi}{\partial r} \qquad (4.5)\\ &= -r^{\lambda-1}\lambda\Big[c_1\sin[(\lambda+1)\theta](\lambda+1)+c_2\cos[(\lambda+1)\theta](\lambda+1)+\\ &\quad +c_3\sin[(\lambda-1)\theta](\lambda-3)+c_4\cos[(\lambda-1)\theta](\lambda-3)\Big];\\ \sigma_{r\theta} &= \frac{1}{r^2}\frac{\partial\Phi}{\partial\theta}-\frac{1}{r}\frac{\partial^2\Phi}{\partial r\partial\theta} \qquad (4.6)\\ &= r^{\lambda-1}\lambda\Big[-c_1\cos[(\lambda+1)\theta](\lambda+1)+c_2\sin[(\lambda+1)\theta](\lambda+1)\\ &\quad -c_3\cos[(\lambda-1)\theta](\lambda-1)+c_4\sin[(\lambda-1)\theta](\lambda-1)\Big].\end{aligned}$$

For all Airy stress functions the equilibrium equations are satisfied automatically. The compatibility condition is satisfied if the Airy stress function fulfills the biharmonic equation, as this approach does.

In this approach, the wedge flanks at $\theta = \pm\alpha$ are traction-free ($\sigma_{\theta\theta} = \sigma_{r\theta} = 0$), leading to $\partial^2\Phi/\partial r^2 = 0$ on the boundary. Comparison of equation (4.3) to (4.4) leads to the observation that $\Phi = 0$ if $\partial^2\Phi/\partial r^2 = 0$. Therefore, the traction-free boundary conditions are fulfilled if

$$\begin{aligned}\Phi(\theta=\pm\alpha) &= 0\\ \frac{\partial\Phi}{\partial\theta}(\theta=\pm\alpha) &= 0\,.\end{aligned}$$

These equations give rise to a linear system of equations,

$$\mathbf{A}\mathbf{c} = \mathbf{0}\,, \qquad (4.7)$$

where $\mathbf{c}$ is the vector of c_i's and the matrix $\mathbf{A}$ is defined by

$$\mathbf{A} = \begin{bmatrix} \sin[\alpha(\lambda+1)] & \cos[\alpha(\lambda+1)] & \sin[\alpha(\lambda-1)] & \cos[\alpha(\lambda-1)] \\ \sin[-\alpha(\lambda+1)] & \cos[-\alpha(\lambda+1)] & \sin[-\alpha(\lambda-1)] & \cos[-\alpha(\lambda-1)] \\ \cos[\alpha(\lambda+1)](\lambda+1) & -\sin[\alpha(\lambda+1)](\lambda+1) & \cos[\alpha(\lambda-1)](\lambda-1) & -\sin[\alpha(\lambda-1)](\lambda-1) \\ \cos[-\alpha(\lambda+1)](\lambda+1) & -\sin[-\alpha(\lambda+1)](\lambda+1) & \cos[-\alpha(\lambda-1)](\lambda-1) & -\sin[-\alpha(\lambda-1)](\lambda-1) \end{bmatrix}.$$

A solution to equation 4.7 other than the trivial solution $c_1 = c_2 = c_3 = c_4 = 0$, requires the determinant of the matrix $\mathbf{A}$ be zero, which is true for

$$(\lambda\sin 2\alpha)^2 = (\sin 2\alpha\lambda)^2. \qquad (4.8)$$

Now let us focus on some energy considerations for the wedge to study the physical boundaries of λ. The energy per unit area in an infinitesimal domain is $dW \propto \sigma^2$. Thus, the energy in a region of radius R around the tip is $W \propto \int_0^R \sigma^2\ 2\pi r\ dr$. Since, $\sigma \propto r^{\lambda-1}$

(see equations (4.4) to (4.6)) and we get $W \propto R^{2\lambda}$. This energy cannot be singular, so that λ has to be greater than zero.

Depending on the wedge angle α, multiple values of λ exist according to equation (4.8), which are shown in figure 4.5. To account for these multiple values the subscript k is introduced.

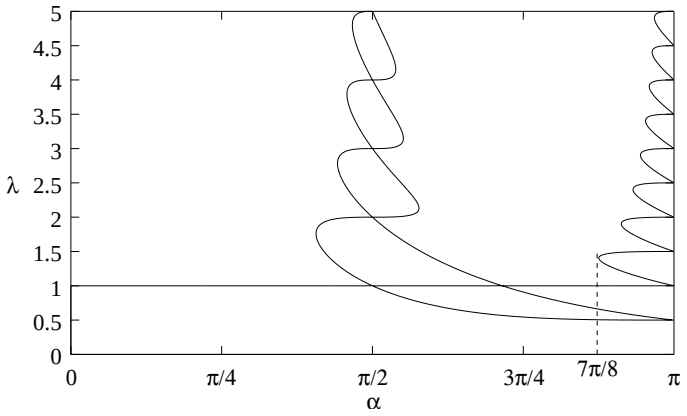

Figure 4.5: Admissible values of λ for wedge angles α between 0 and π.

Keeping in mind the remarks about the self similarity of elastic fields from the beginning of this section, equations (4.4) to (4.6) can be rewritten, similar to the solution for an infinitely sharp crack, as

$$\begin{aligned} \boldsymbol{\sigma} &= \sum_k r^{\lambda_k - 1} K_k \overset{*}{\boldsymbol{f}}_k (\lambda_k, \theta) \\ K_k &= a_k \sigma_{\mathrm{app}} h^{1-\lambda_k}. \end{aligned} \tag{4.9}$$

$\overset{*}{\boldsymbol{f}}_k$ are the unit versions of $\boldsymbol{f}_k$ (see equation (4.2)) and a_k are non-dimensional scalars, which have to be fitted. σ_{app} is the uniform applied stress and h is the surface step height, as shown in figure 4.1.

$\lambda_k = 1$ is a solution for all wedge angles α. The corresponding c_i's of equation (4.3) are $[0, 0, 1, 0]$. This leads to $\Phi = 0$ and $\partial\Phi/\partial\theta = 0$ for all θ, which in turn leads to all stress components vanishing everywhere in the domain. Therefore, $\lambda_k = 1$ is a trivial solution and will not be considered any further.

Having excluded the solution $\lambda_k = 1$, an even number of solutions exist for almost all wedge angles α, as shown in figure 4.5. Determining $\mathbf{c}_k$ from equation (4.7), one finds that either c_{1k} and c_{3k} are zero or that c_{2k} and c_{4k} are zero. Furthermore, according to equations (4.4) and (4.5) c_1 and c_3 are the pre-factors to the sine while c_2 and c_4 correspond

to the cosine for $\sigma_{\theta\theta}$ and σ_{rr}. For the shear component it is vice versa. Therefore, half of these solutions result into symmetric stress fields with respect to the ξ axis (see figure 4.4), the other half into antisymmetric fields.

For the representative surface step, i.e. $\alpha = 7/8\,\pi$, so that $2(\pi - \alpha) = \pi/4$, two values of λ_k can be determined by figure 4.5, for each of which the vector $\overset{*}{\mathbf{c}}_k$ is calculated according to equation (4.7), (the star denotes that the vector is a unit vector). This leaves the coefficients a_k of equation (4.9) as the only fitting parameters. We fit the resulting expressions for the stress fields to the results obtained by FEM, as shown in figure 4.2. Figure 4.6 gives the resulting distribution of σ_{xx} and σ_{yy}.

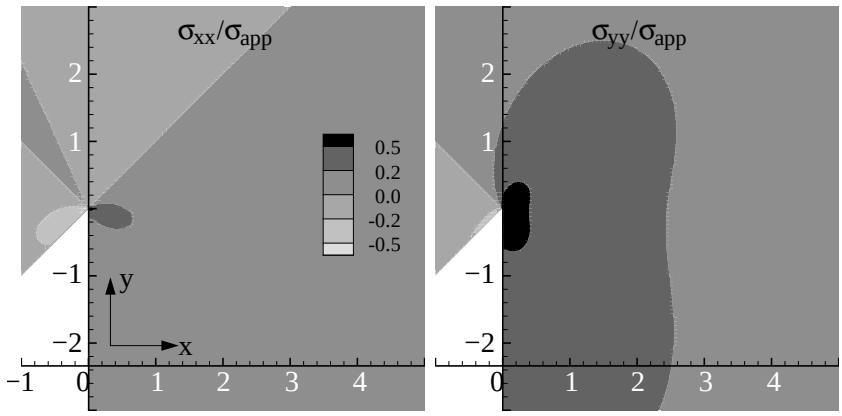

(a) (b)

Figure 4.6: First approximation of the stress distribution near a surface step using the wedge solution with traction-free boundary conditions. Stress components in the x-direction (a) and in the y-direction (b).

Comparison with figure 4.2 reveals that there are points of agreement and disagreement. The stress component σ_{xx} is matched quite well, except at points close to the upper terrace (see figure 4.1). These points have a negative x-coordinate as shown in figure 4.1 and, therefore, lie outside the region of analysis for the small-strain formulation of the dislocation dynamics model, where this approach is to be used. Therefore, the difference of this first approach to the numerical solution is not significant. However, the stress component in the y-direction does not show such a good agreement and overestimates the stresses determined by FEM.

The differences of this approach to the FEM solution arise because the upper surface terrace (see figure 4.1) is not taken into account by this approach (cf. also dashed line in figure 4.4). Only the lower terrace and the step are accounted for. The influence of the upper surface terrace on the elastic fields is strong in the area shown in figure 4.6 because the surface step height is on the same order of length as the size of the area of interest.

Therefore, St. Venant's principle indicates that the stresses at the wedge are influenced by the upper surface terrace.

However, the general shape of the distributions of both stress components is in fair agreement with the FEM solution. A second approach is given in the following subsection which attempts to avoid the problem of this approach.

4.2.4 Approximation using the wedge solution with traction boundary conditions

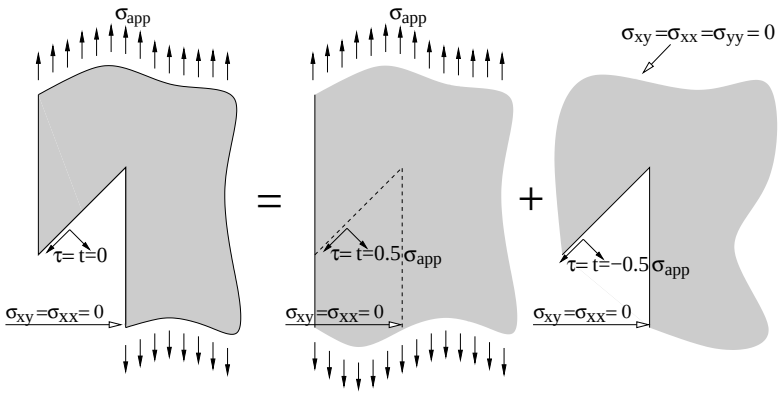

Figure 4.7: Second approach to approximate the elastic fields of a surface step.

In figure 4.7 the second approach is shown, where the elastic field due to a surface step is modeled as a uniform half-space from which a wedge is removed. This leads to one zero and one non-zero traction boundary condition on the wedge. The tractions on the lower terrace are zero, since the uniform applied stress is parallel to this line. However, the tractions on the step are given by Mohr's circle as half of the uniform applied uniaxial stress since the wedge has an angle of $45°$.

Equations (4.2) to (4.6) of the previous subsection apply also for this approach. However, because there are tractions on one side of the wedge, as shown in figure 4.7, the right-hand side of equation 4.7 is non-zero in this case. We call the right-hand side vector $\mathbf{b}$, which incorporates the boundary conditions. The solution of the equation $\mathbf{Ac} = \mathbf{b}$ reads

$$\mathbf{c} = \frac{1}{4}\sigma_{\text{app}} \begin{vmatrix} \dfrac{\cos[(\lambda-1)\alpha](\lambda-1)+\sin[(\lambda-1)\alpha]}{\cos[(\lambda-1)\alpha]\sin[(\lambda+1)\alpha](\lambda-1)-\cos[(\lambda+1)\alpha]\sin[(\lambda-1)\alpha](\lambda+1)} \\ \dfrac{\sin[(\lambda-1)\alpha](\lambda-1)-\cos[(\lambda-1)\alpha]}{\cos[(\lambda-1)\alpha]\sin[(\lambda+1)\alpha](\lambda+1)-\cos[(\lambda+1)\alpha]\sin[(\lambda-1)\alpha](\lambda-1)} \\ \dfrac{-\cos[(\lambda+1)\alpha](\lambda+1)-\sin[(\lambda+1)\alpha]}{\cos[(\lambda-1)\alpha]\sin[(\lambda+1)\alpha](\lambda-1)-\cos[(\lambda+1)\alpha]\sin[(\lambda-1)\alpha](\lambda+1)} \\ \dfrac{-\sin[(\lambda+1)\alpha](\lambda-1)-\cos[(\lambda+1)\alpha]}{\cos[(\lambda-1)\alpha]\sin[(\lambda+1)\alpha](\lambda+1)-\cos[(\lambda+1)\alpha]\sin[(\lambda-1)\alpha](\lambda-1)} \end{vmatrix}$$

Notice, **c** depends only on a single λ, which in this approach is a fitting parameter. Furthermore, $\lambda < 1$ if there is a stress singularity at the surface step. However from the energetic considerations of the previous approach, $\lambda > 0$. Therefore, one does not have much freedom in fitting the solution of this approach to the numerical result. Figure 4.6 shows the stress distribution for the second approximation with $\lambda = 0.8$.

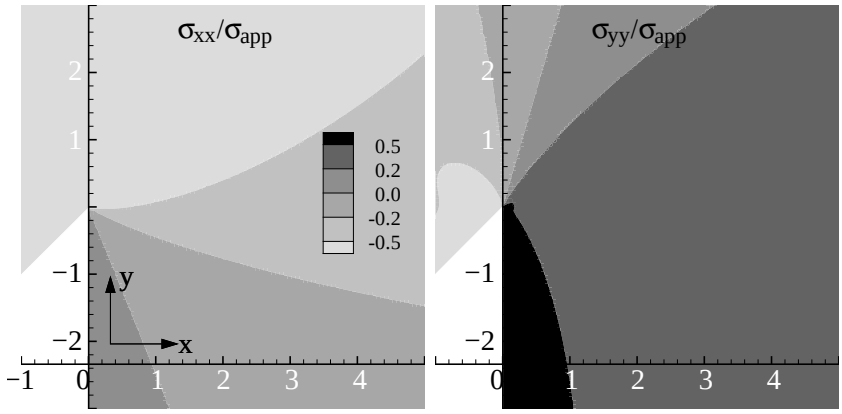

(a) (b)

Figure 4.8: Second approximation of the stress contours of the surface step using the wedge solution with non-traction-free boundary conditions. Stress components in the x-direction (a) and in the y-direction (b).

Comparing the results shown in figure 4.8 to those in figure 4.2, one finds more differences than with the first approach. For instance, the numerical solution of σ_{xx} reveals a butterfly-like stress distribution around the singularity at the tip; but this is not observed in figure 4.8 (a). Notice, σ_{xx} is equal to zero at the lower terrace, as prescribed by the boundary condition in figure 4.7. However, this is not shown by the contours in figure 4.8 due to the strong gradient in σ_{xx} and the rough mesh. Moreover comparing this approach

to the numerical calculation, σ_{yy} has much higher values here, because the highest stress contour extends to the bottom of figure 4.8.

Differences to the numerical result arise because the upper terrace (see figure 4.1) is also not taken into account in this approach, while the lower is. Therefore, the traction is non-zero along the upper terrace. For that reason the remarks given at the end of the previous subsection about the area influenced by the surface step also apply in this approach. Differences to the previous approach originate from the fast that the latter involves homogeneous boundary conditions and therefore a decrease of the rank of matrix **A**, which leads to two variables a_1 and a_2 being fit parameters. In this approach, however, only a single value λ is fitted.

4.2.5 Third approximation using the crack solution

In the third approach the elastic solution for an infinitely sharp crack is used to model the stress concentration at the surface step as shown in figure 4.9. Towards this end, the representative surface step (see figure 4.9 (a)) is copied, rotated by $180°$ (see figure 4.9 (b)) and glued to the first piece along the upper and lower surface terrace (see figure 4.9 (c)).

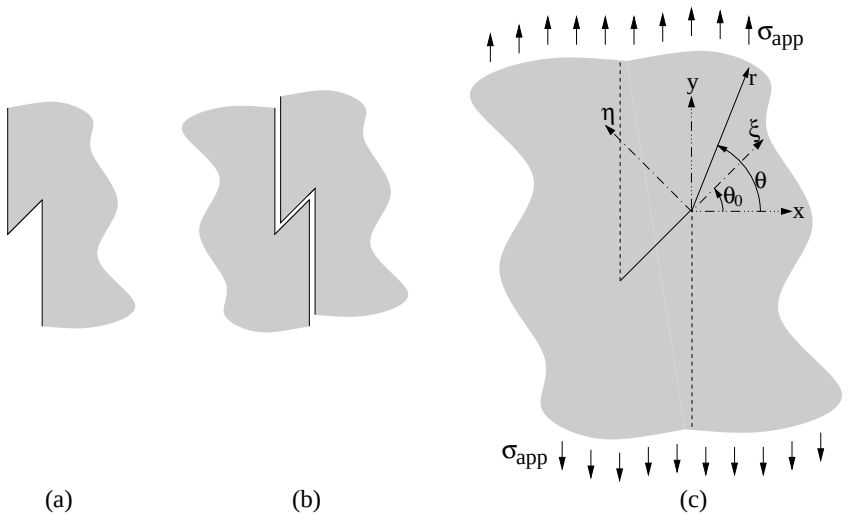

Figure 4.9: Surface step (a), copied and rotated surface steps before glueing them together (b). Definitions used for this approach (c).

The dashed line in figure 4.9 (c) marks the glue. Along the step, i.e. the diagonal line, no glue is applied. The result of this sequence is a diagonal, $h\sqrt{2}$ long, infinitely-sharp crack in infinite space.

The crack as shown in figure 4.9 (c) is subjected to mixed mode I – II loading such that the combined stress gives $\sigma_{yy}^{\infty} = \sigma_{\text{app}}$ and $\sigma_{xx}^{\infty} = \sigma_{xy}^{\infty} = 0$. The stress fields near a mode I and mode II crack are (see, for instance, [50])

$$\begin{aligned}
\sigma_{\xi\xi} &= \frac{K_I}{\sqrt{2\pi r}} \cos\frac{\phi}{2}\left(1 - \sin\frac{\phi}{2}\sin 3\frac{\phi}{2}\right) + \frac{K_{II}}{\sqrt{2\pi r}} \sin\frac{\phi}{2}\left(-2 - \cos\frac{\phi}{2}\cos 3\frac{\phi}{2}\right) \\
\sigma_{\eta\eta} &= \frac{K_I}{\sqrt{2\pi r}} \cos\frac{\phi}{2}\left(1 + \sin\frac{\phi}{2}\sin 3\frac{\phi}{2}\right) + \frac{K_{II}}{\sqrt{2\pi r}} \sin\frac{\phi}{2}\left(\cos\frac{\phi}{2}\cos 3\frac{\phi}{2}\right) \\
\sigma_{\xi\eta} &= \frac{K_I}{\sqrt{2\pi r}} \cos\frac{\phi}{2}\left(\sin\frac{\phi}{2}\cos 3\frac{\phi}{2}\right) + \frac{K_{II}}{\sqrt{2\pi r}} \cos\frac{\phi}{2}\left(1 - \sin\frac{\phi}{2}\sin 3\frac{\phi}{2}\right) .
\end{aligned}$$

The stress intensity factors K_I and K_{II} are determined by the resolved normal and tangential stress (both $1/2\,\sigma_{\text{app}}$ for a $\theta_0 = 45°$ wedge) according to the first order estimate:

$$\begin{aligned}
K_I &= 0.5\sigma_{\text{app}}\sqrt{\pi\sqrt{2}h} \\
K_{II} &= 0.5\sigma_{\text{app}}\sqrt{\pi\sqrt{2}h},
\end{aligned}$$

The interaction of the tip at $x = -h$, $y = -h$ is neglected because there, i.e. at the tip of the wedge, a singularity is unphysical. Note, there is no fitting involved in this approach. The resulting distribution of σ_{xx} and σ_{yy} are shown in figure 4.10.

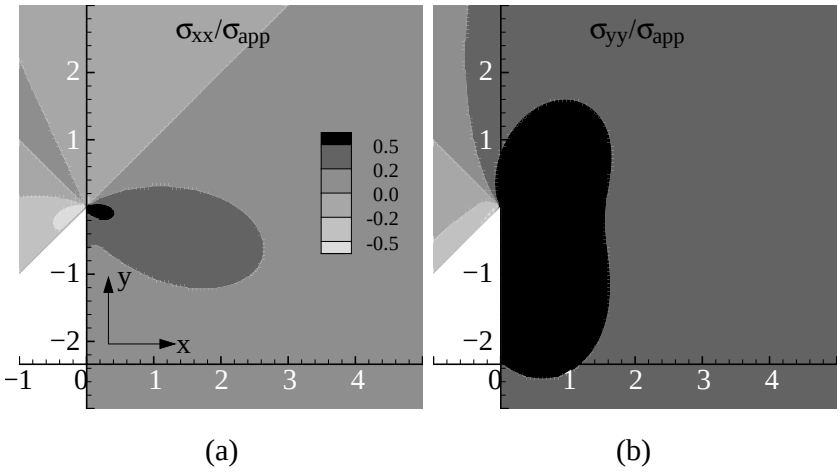

Figure 4.10: Combined mode I and II crack solutions are used as an approximation of the stress fields of the surface step. Stress components in the x-direction σ_{xx} (a) and in the y-direction σ_{yy} (b).

Comparing figure 4.2 to figure 4.10 the stress component in the x-direction close to the tip is higher than for the numerical solution. Furthermore, σ_{xx} is not zero at the lower terrace, as one can see from the contours in figure 4.10 intersecting the lower terrace. However, this surface is traction free. The reason for the unphysical stress distribution lies in the glueing together of the upper and lower surface terrace. The surfaces in figure 4.9 (b) are traction free, but this is lost once the pieces are glued together to become the configuration shown in figure 4.9 (c). Moreover, in this approach the stress component in the y-direction is substantially higher than the numerical result and also higher than the analytical result of the first approach.

After having tested three novel approaches to approximate the results obtained by FEM for the representative surface step, we now look at some approaches given in literature.

4.2.6 Comparison with existing solutions

When growing crystals by atom vaporization, flat surface islands, i.e. terraces, develop (see, e.g., [51]). Based on the surface stress of the crystal Marchenko and Parshin [52] have suggested the following scaling relation for all stress components for a surface step of arbitrary shape:

$$\boldsymbol{\sigma} \propto \frac{1}{\sqrt{r}} \tag{4.10}$$

where r is the distance from the surface step. Since Marchenko and Parshin do not give the pre-factors nor the angular dependence, the figure shows only a qualitative picture. Therefore, the shape and the values of the stress contours are arbitrary. Nothing can be said about the boundary conditions at the free surface, because the angular dependence could satisfy them. However, the solution given by Marchenko and Parshin predicts a stress field which decays with $\sqrt{r}$, which is the same as for an infinitely sharp crack. Our first approach (section 4.2.3) predicts two exponents for the stress, i.e. $\lambda_1 - 1 = 0.49$ and $\lambda_2 - 1 = 0.35$. The first exponent is very close to the Marchenko and Parshin value of 0.5.

Kukta and Bhattacharya [51] have extended the model of Marchenko and Parshin [52] to model atom vaporization on a specimen under tension. Therefore, they calculated the stress fields for surface steps with an elastic background stress. This extension makes the solution quite long and difficult. Nevertheless, still the surface energy dominates, which is the dominating part for atom vaporization. However, supported by the experimental findings by Forsyth [53] and Cottrell and Hull [54] of long and very thin sheets of extrusions, the surface energy apparently is not dominant.

Brochard et al. [55] gave a different solution based on the point force approach of Boussinesq (see, e.g. [56]). Here, with a stress along the surface step the finite-width specimen is in equilibrium, as shown in figure 4.11 (a). Afterwards, the stress at the surface step is idealized as a point force $F = \sigma_{\mathrm{app}} h$, which is applied at the surface of the half-space, as shown in figure 4.11 (b). According to the Boussinesq solution, the stress distribution is

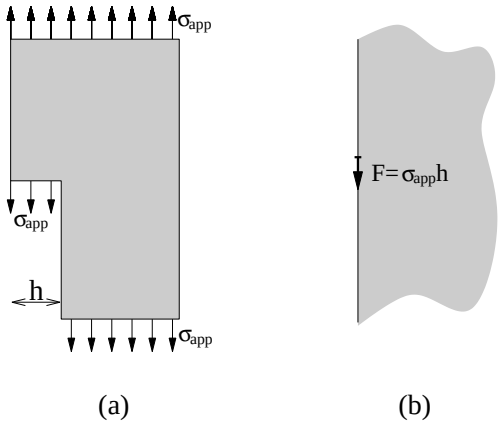

Figure 4.11: Surface step in equilibrium (a). Idealization to a point force (b).

given by

$$\begin{aligned} \sigma_{rr} &= -\frac{2}{\pi}\sigma_{\mathrm{app}} h \frac{\sin\theta}{r} \\ \sigma_{\theta\theta} = \sigma_{r\theta} &= 0 \end{aligned}$$

with (r, θ) a cylindrical coordinate system at the point of application of the point force.

This solution is very simple and satisfies the equilibrium, compatibility and the boundary conditions on the wedge flanks except of at the upper terrace. The corresponding stress distribution is shown in figure 4.12. The solution predicts equally high stresses in the x- and y-direction. This is not in agreement with the numerical solution where the stress component in the y-direction is dominating (see figure 4.2). In this approach the surface step is idealized as a point. This idealization of a step to a point does not influence the stress fields far away from the surface step. However, for points very close to the surface step, i.e. the area shown in figure 4.12, this idealization is not fair. The distance of these points to the surface step is on the same order as the surface step height. Therefore, St. Venant's principle predicts a change in the elastic fields in the area due to a change in the shape of the surface step.

Furthermore, the surface step is traction-free if a material with a surface step is subjected to tension. This observation results in the applied stresses at the ends of the body not being equal. Therefore, the assumption of Brochard that there are stresses along the surface step is not physical.

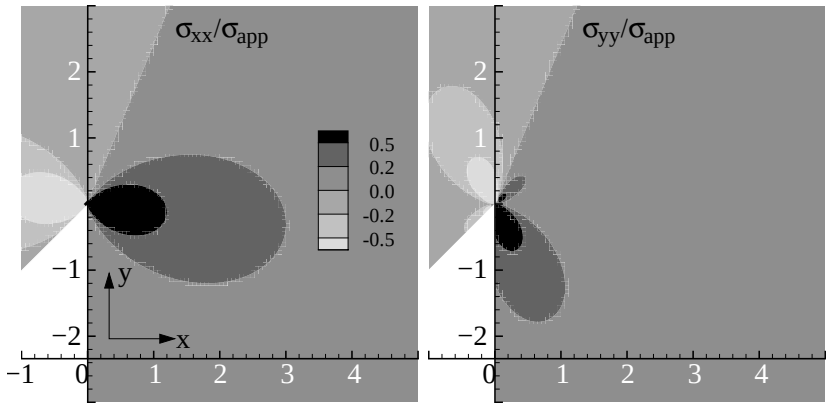

(a) (b)

Figure 4.12: Stress contours of the elastic fields of a surface step according to Brochard et al. [55]. Stress components in x-direction (a) and in y-direction (b).

4.2.7 Concluding remarks on step modeling

None of the analytical solutions mentioned here is in perfect agreement with the numerical solution. No model captures the free surface boundary conditions at the upper terrace. Some models even fail to take the free surface at the lower terrace into account. The models given in literature are either based on surface tension or on the assumption that a stress is applied at the surface step. Neither is relevant for fatigue. Moreover, all models predict higher stresses than the numerical computation. Nevertheless, in order to have a workable approximation, we choose to adopt the first approach because it shows most similarity with the numerical solution for both stress components.

To further investigate the quality of the first approximation, figure 4.13 shows the normalized stress component $\sigma_{yy}/\sigma_{\mathrm{app}}$ against the normalized coordinate x/h in a log-log diagram for a surface step with an opening angle of 45°, i.e. $\alpha = 7/8\ \pi$. For equilibrium both negative and positive stress components σ_{yy} have to be present along the x-axis, as shown by the numerical and the analytical solution, i.e. both curves cross the x-axis at around $x/h = 8$.

Furthermore, close to the wedge tip ($x = 0$) the slope of the numerical curve is very close to $-1/2$, which is the analytical value for an infinitely sharp crack. For increasing x the slope decreases fast for the FEM solution and somewhat slower in the analytical solution. In conclusion, the analytical approximation overestimates the stress compared to the numerical solution for points far away from the surface step, but otherwise gives a fair correspondence, as shown in figure 4.13.

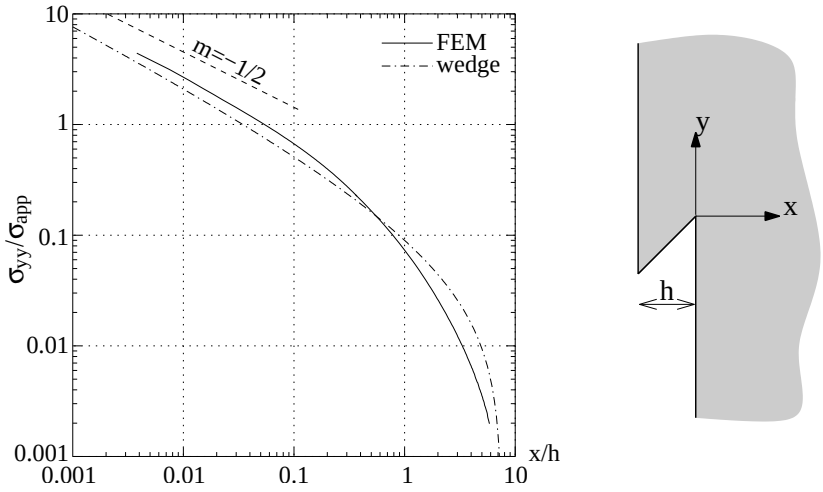

Figure 4.13: Surface step-induced stress profile σ_{yy} into the crystal according to the numerical 'FEM' and analytical 'wedge' solution. h is the step height of the surface step.

Displacement fields

To account for the opening of the cohesive surface, which we will use in chapter 6, the displacement fields are calculated. The constitutive equations for cylindrical coordinates are similar to those for Cartesian coordinates and in plane strain (see, for instance, [57]) read

$$\begin{aligned}
\varepsilon_{rr} &= \frac{1+\nu}{E}[(1-\nu)\sigma_{rr} - \nu\sigma_{\theta\theta}]; \\
\varepsilon_{\theta\theta} &= \frac{1+\nu}{E}[-\nu\sigma_{rr} + (1-\nu)\sigma_{\theta\theta}]; \\
\varepsilon_{r\theta} &= \frac{1+\nu}{E}\sigma_{r\theta}
\end{aligned}$$

In addition, the strain-displacement relationships read (see, for instance, [57])

$$\begin{aligned}
\varepsilon_{rr} &= \frac{\partial u_r}{\partial r} \\
\varepsilon_{\theta\theta} &= \frac{u_r}{r} + \frac{\partial u_\theta}{\partial \theta} \\
\varepsilon_{r\theta} &= \frac{1}{2}\left(\frac{1}{r}\frac{\partial u_r}{\partial \theta} + \frac{\partial u_\theta}{\partial r} - \frac{u_\theta}{r}\right)
\end{aligned}$$

Substitution of the stress field equation (4.9) and integration leads to the displacement fields for the surface step,

$$\begin{aligned} u_r &= \frac{1+\nu}{E}\sum_k r^{\lambda_k} K_k R_k(\lambda_k,\theta); \\ u_\theta &= \frac{1+\nu}{E}\sum_k r^{\lambda_k} K_k \Theta_k(\lambda_k,\theta)\,. \end{aligned}$$

where the coefficients R_k and Θ_k are given by

$$\begin{aligned} R_k &= c_{1k}\sin[(\lambda_k+1)\theta](\lambda_k+1) + c_{2k}\cos[(\lambda_k+1)\theta](\lambda_k+1) + \\ &\quad c_{3k}\sin[(\lambda_k-1)\theta](\lambda_k+1-4\nu) + c_{4k}\cos[(\lambda_k-1)\theta](\lambda_k+1-4\nu) \end{aligned}$$

$$\begin{aligned} \Theta_k &= (\lambda_k-1)\Big[-c_{1k}\cos[(\lambda_k+1)\theta] + c_{2k}\sin[(\lambda_k+1)\theta] - \\ &\quad c_{3k}\cos[(\lambda_k-1)\theta]\frac{\lambda_k+1-4\nu}{\lambda_k-1} + c_{4k}\sin[(\lambda_k-1)\theta]\frac{\lambda_k+1-4\nu}{\lambda_k-1}\Big] \end{aligned}$$

where K_k is given by equation (4.9) and was determined by fitting the expressions for the stress fields to the numerical solution. λ_k and c_{1k} to c_{4k} are given by equations (4.8) and (4.7), respectively. The subscript k denotes the multiple values of λ for a given α from equation (4.8).

Both displacement components increase with the radius r from the wedge since $\lambda_k > 0, \forall k$. For a physical solution the integration constant would have to be identified such that the additional displacement to the uniform background displacement is zero at the boundary of the body. The value of the integration constants is irrelevant for the cohesive surface model since we are interested in the opening, i.e. in the difference of the displacement between both sides of the cohesive surfaces where the integration constant cancels out.

4.3 Application to dislocation model

Stress field

To account for the change in the stress field due to the surface roughness on dislocation nucleation and movement, the stress fields of the discrete surface steps are added to the other stress components $(\tilde{\boldsymbol{\sigma}}+\hat{\boldsymbol{\sigma}})$, as already introduced in equation (4.1), which is repeated here for completeness:

$$\begin{aligned} \boldsymbol{\sigma} &= \tilde{\boldsymbol{\sigma}} + \hat{\boldsymbol{\sigma}} + \bar{\boldsymbol{\sigma}} \\ &= \tilde{\boldsymbol{\sigma}} + \hat{\boldsymbol{\sigma}} + \sum_l \bar{\boldsymbol{\sigma}}_l \end{aligned}$$

Adoption to slip systems of our model

In the dislocation dynamics simulation described in chapter 2 three discrete slip systems

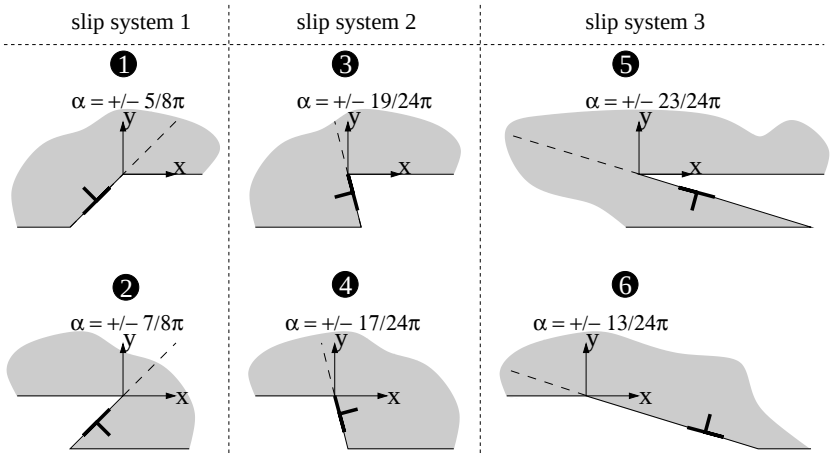

Figure 4.14: Six cases of surface steps for three slip systems. The top row depicts the cases for positive steps; the bottom row for negative steps. The dashed line marks the slip plane. The magnitude of the Burgers vector has been scaled so that the step height h is the same in all cases.

are used, which can have either a positive or negative step at the free surface. This leads to six unit cases shown in figure 4.14. The first slip system is favorably oriented for plastic slip at $\pi/4$ and is shown in the first column. The values of λ_k (see, equation (4.9)) and $\overset{*}{c}_{ik}$, which are the unit vectors of c_{ik} (see, equation (4.3)) are

slip system	case	α	λ	$\overset{*}{c}_1$	$\overset{*}{c}_2$	$\overset{*}{c}_3$	$\overset{*}{c}_4$
1	1	$5/8\ \pi$	0.674	0.000	0.629	0.000	0.777
			1.302	0.495	0.000	0.869	0.000
	2	$7/8\ \pi$	0.505	0.000	0.358	0.000	0.934
			0.660	0.631	0.000	-0.776	0.000
2	3	$19/24\ \pi$	0.525	0.000	0.430	0.000	0.903
			0.813	0.416	0.000	-0.909	0.000
	4	$17/24\ \pi$	0.574	0.000	0.529	0.000	0.849
			1.019	0.044	0.000	0.999	0.000
3	5	$23/24\ \pi$	0.500	0.000	0.321	0.000	0.947
			0.545	0.700	0.000	-0.714	0.000
			1.091	0.000	0.694	0.000	-0.720
			1.499	0.000	0.206	0.000	-0.979

slip system	case	α	λ	$\overset{*}{c}_1$	$\overset{*}{c}_2$	$\overset{*}{c}_3$	$\overset{*}{c}_4$
3	5	$23/24\ \pi$	1.638	0.686	0.000	-0.728	0.000
			1.997	0.337	0.000	-0.942	0.000
			2.187	0.000	0.678	0.000	-0.735
			2.492	0.000	0.426	0.000	-0.905
			2.740	0.667	0.000	-0.745	0.000
			2.984	0.491	0.000	-0.871	0.000
			3.301	0.000	0.653	0.000	-0.757
			3.467	0.000	0.546	0.000	-0.838
	6	$13/24\ \pi$	0.857	0.000	0.697	0.000	0.717
			1.711	0.685	0.000	0.729	0.000
			2.007	0.000	0.339	0.000	0.941
			2.557	0.000	0.671	0.000	0.741
			3.035	0.497	0.000	0.868	0.000
			3.379	0.650	0.000	0.760	0.000

To investigate the influence of the surface step opening angle $2(\pi - \alpha)$ on the stress field, a series of numerical calculations is executed. The additional stress to the uniform background stress is shown in figure 4.15 for some point P within a distance h from the wedge tip. Over a wide range of wedge opening angles the stress is almost constant. When $\alpha \to \pi/2$, i.e. the flat surface without any stress singularity, the additional stress to the

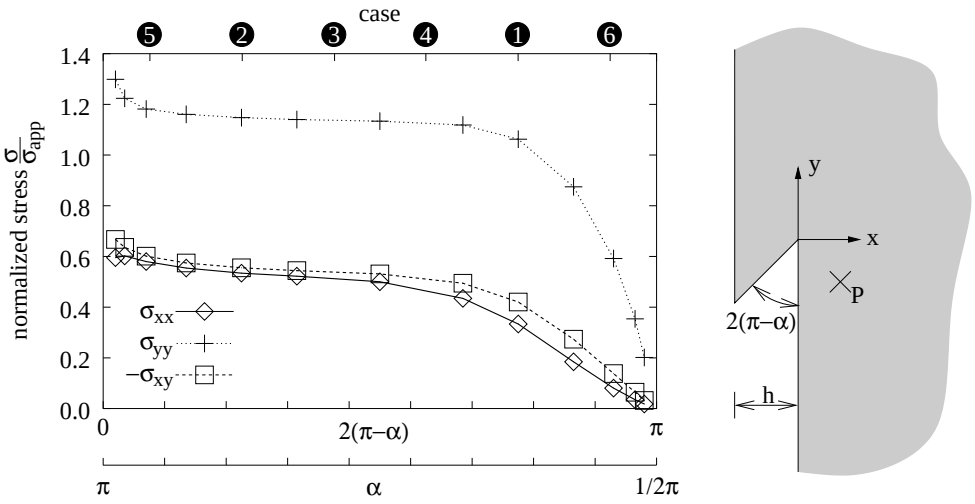

Figure 4.15: Numerical calculation: Additional stress to the uniform background stress σ_{app} at point $P = (3/5\ h; -3/5\ h)$.

uniform background stress approaches zero. However, when α increases these stresses increase. This result agrees to the finding of Repetto and Ortiz [18]; the fatigue crack is most likely to nucleate from the acute angle of the PSB with he surface. However, between the extreme configurations, the stresses can be considered constant. Because almost all 6 cases lie inside the constant region, especially those of the primary slip systems, i.e. cases 1 and 2, all surface steps shown in figure 4.14 will be treated in the sequel as case 2, i.e. with $\alpha = 7/8\ \pi$.

Comparisons of the analytical to the numerical solution for a complex surface structure

After having looked at a single surface step we now focus on a more realistic surface roughness with hundreds of surface steps. There is no assumption on the evolution of surface roughness. It is an outcome of the dislocation dynamics simulation, in which we track the number of dislocations moving out for each slip plane individually. Based on these numbers we calculate the step heights and the elastic fields due to the surface steps. The calculation of the elastic fields at every time step of the simulation is very expensive. To accelerate the calculation for complex surface structures with many surface steps, the applicability of a cut-off radius is investigated. The results for a $1\mu\mathrm{m} \times 2\mu m$ grain after 500 stress cycles are shown in figure 4.16.

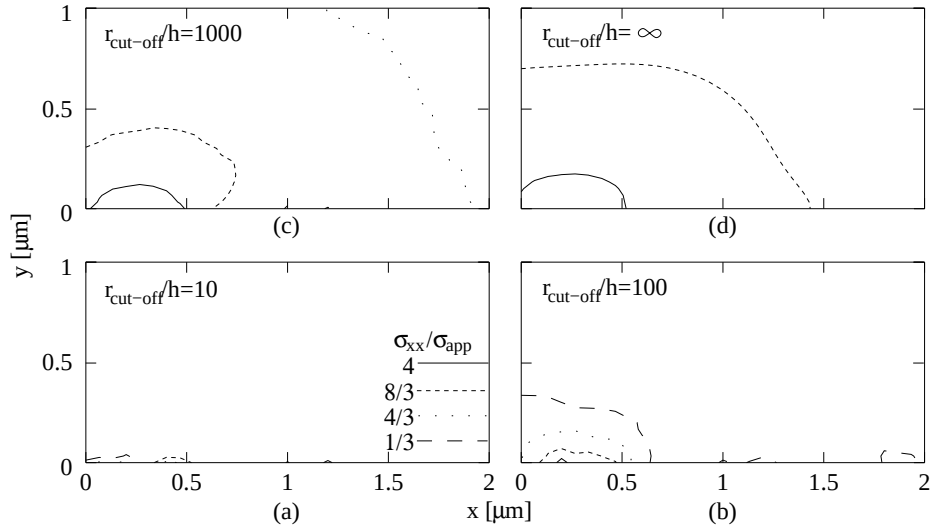

Figure 4.16: The influence of a cut-off radius on the stress distribution $\sigma_{xx}/\sigma_{\mathrm{app}}$ inside a $1\mu\mathrm{m} \times 2\mu\mathrm{m}$ grain caused by the surface roughness after 500 stress cycles. The surface roughness was simulated by the 2DD model and is similar to that in figure 2.10 (a).

In figure 4.16 the grain is shown after 500 stress cycles with the free surface along $y = 0$ and the applied stress parallel to the free surface. According to St. Venant's principle the elastic fields are altered by the surface step in an area which has a size on the order of the surface step height. We use $r_{\mathrm{cutoff}}/h = 10$, $r_{\mathrm{cutoff}}/h = 100$ and $r_{\mathrm{cutoff}}/h = 1000$ to investigate the influence of a cut-off radius. For those cut-off radii, there is a significant difference in the stress distribution compared to that without a cut-off. In conclusion, the cut-off radii underestimates the effect of the surface steps significantly. This can be understood by recalling that in figure 4.6 the analytical approach predicts that the stress decays rapidly; the radius of the $1/2\sigma_{\mathrm{app}}$ contour is smaller than h. However, there are a great number of steps along the surface after 500 cycles. This defines the width of the grain as the characteristic length for St. Venant's principle. Therefore, the region with an influence in the stress field due to the surface roughness is characterized by the size of the grain.

Now we compare the analytical solution to the numerical one for a complex surface structure. The 2DD model described in chapter 2 is used to calculate a surface roughness for a $2\mu\mathrm{m} \times 2\mu\mathrm{m}$ grain. For convenience of mesh generation, a sample of that surface profile is simplified, i.e. small ex- and intrusions are deleted from the profile. Subsequently, an elastic FEM calculation is performed that will only reveal the stress field caused by the surface steps. Figure 4.17 shows the stress distribution for a coarse mesh, which gives only a crude approximation to the elastic fields caused by the surface roughness. Therefore, the stress distribution is different than the result for the single step shown in figure 4.2. Moreover, only a few contours are shown in figure 4.17. Comparing figure 4.17 to figure 4.16 (d), the area with a stress enhancement of $1/3\sigma_{\mathrm{app}}$ due to the surface roughness is much smaller for the numerical solution than for the analytical solution. Moreover, the stress enhancement close to the free surface is smaller for the numerical than for the analytical solution.

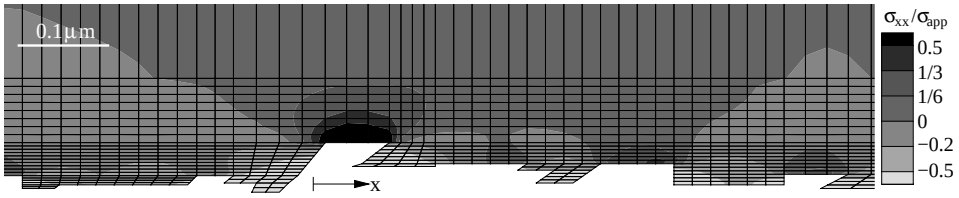

Figure 4.17: Stress enhancement in the x-direction $\sigma_{xx}/\sigma_{\mathrm{app}}$ under tensile loading in the x-direction at a particular surface roughness, which is similar to the surface roughness used for figure 4.16.

Evolution of stress due to accumulation of surface roughness

The stress in the grain due to the surface roughness is determined, according to equation (4.9), by the height of the surface roughness and the background stress. In figure 4.18 the evolution of the surface roughness, i.e. the sum of the heights of the surface steps, is shown for a $2 \times 1\mu m$ grain using the 2DD model explained in chapter 2. Like the dislo-

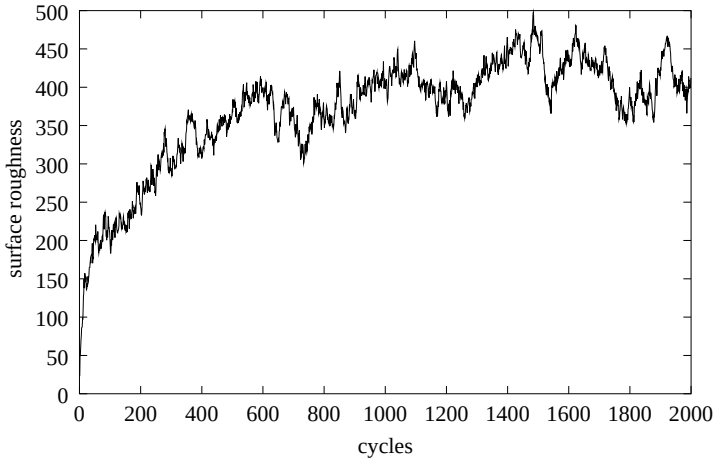

Figure 4.18: The evolution of the total surface roughness $\sum h_i/b$ for a $2 \times 1\mu m$ grain for 2000 cycles using the 2DD model described in chapter 2. h_i denotes the height of the individual surface steps.

cation density, which is shown in figure 2.15, the surface roughness is increasing rapidly at the beginning and starts to level off after 600 cycles. Evidently, surface roughness and dislocation density are connected. If a slip plane, which is bound on one side by the free surface, has an impenetrable grain boundary on the other end, the surface roughness stops growing once the number of dislocations on the slip plane stops increasing, which is evident by the comparison of figures 2.15 and 4.18.

The second parameter determining the stress caused by surface roughness is the background stress, i.e. the applied stress σ_{app} for the representative surface step in section 4.2. In figure 4.19 the evolution of the average and the standard deviation of $\tilde{\sigma}_{xx}$ along the free surface is shown (recall that $\tilde{\sigma}_{xx}$ is the stress caused by the singular fields of all dislocations). Because the dislocation density does not evolve monotonically but with large oscillations $\tilde{\sigma}_{xx}$ also oscillates. For the 2000 cycles shown, the average stress along the free surface is roughly a third of the peak applied stress. However, the standard deviation increases during time. This leads to an increase in the instantaneous local background stresses σ_{app}, which acts on the discrete surface steps. This local increase in the stress could lead, if other conditions are satisfied, to crack initiation which is also a local phenomena.

In conclusion, the stress due to the surface roughness increases over time since both the surface roughness and the local stresses at the free surface increase. The elastic fields in the entire grain are influenced by the surface roughness and the stress enhancement due to the surface steps is on the order of the applied stress. This leads to the final conclusion that the region of influence and the enhancement in the stress due to surface roughness are quite substantial in initiating fracture.

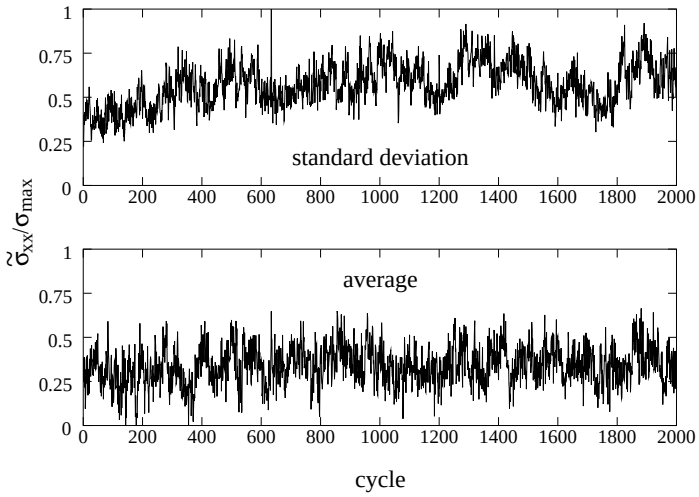

Figure 4.19: The evolution of the average and standard deviation of the stress component $\tilde{\sigma}_{xx}/\sigma_{\max}$ along the free surface for 2000 cycles. This stress is due to the dislocation distribution in a $2\mu\mathrm{m} \times 1\mu\mathrm{m}$ grain using the 2DD model explained in chapter 2. $\sigma_{\max}$ is the maximal applied stress (cf. figure 2.1)